Article

Copyright © 2018 American Scientific Publishers
All rights reserved
Printed in the United States of America

Journal of
Biomedical Nanotechnology
Vol. 14, 1208–1224, 2018
www.aspbs.com/jbn

Targeting Delivery of Rapamycin with Anti-Collagen IV Peptide Conjugated Fe_3O_4@Nanogels System for Vascular Restenosis Therapy

Qian Yang[1,*], Jinrong Peng[2], Chan Chen[3], Yao Xiao[2], Liwei Tan[4], Xingliang Xie[1], Xiaohong Xu[1], and Zhiyong Qian[2,*]

[1] *School of Pharmacy, Collaborative Innovation Center of Sichuan for Elderly Care and Health, Sichuan Province College Key Laboratory of Structure-Specific Small Molecule Drugs, Chengdu Medical College, No. 783, Xindu Avenue, Xindu District, Chengdu 610500, Sichuan, P. R. China*
[2] *State Key Laboratory of Biotherapy, West China Hospital, and Collaborative Innovation Center of Biotherapy, Sichuan University, Chengdu 610041, Sichuan, P. R. China*
[3] *Department of Anesthesiology, West China Hospital of Sichuan University, Chengdu 610041, Sichuan, P. R. China*
[4] *College of Medicine, Southwest Jiaotong University, Chengdu 610031, Sichuan, P. R. China*

Coronary arterial disease (CAD) remains the leading cause of death globally. Although percutaneous coronary interventions (PCI) are most of the important clinical procedure for CAD treating, unfortunately, vascular restenosis is proved as the major drawback of PCI. Because of the complex nature of the restenotic process, the efficacy of drug administration is emphasized. Targeting drug delivery systems become a promising experimental approach for restenosis therapy. Hence, we design and fabricate a thermo/pH-responsive nanogel system with the magnetic inner core as the multifunctional nanocarrier for drug delivery and MRI/fluorescence imaging. To this end, NIPAm-based Fe_3O_4 core–shell structure nanogel is synthesized as the responsive nanosystem for rapamycin (RAPA) delivery, and the surface conjugation with anti-collagen IV peptide makes the nanosystem an ideal candidate for targeting delivery of RAPA. Based on its stimuli-responsive properties, the nanosystem shows desirable intracellular release behavior of RAPA and significantly reduces the adverse effect of RAPA. The *in vitro* cytotoxicity evaluations present the biosafety profiles and antiproliferation performance of the drug-loaded nanogels. Meanwhile, the magnetic Fe_3O_4 inner core shows enhanced T_2 weight sensitivity, providing a high potential for imaging-guiding therapy. In the balloon angioplasty model, targeting nanogels are demonstrated accumulation at the injured site of artery. Compared with the non-targeting nanogels, treatment with peptide conjugated nanogels attenuates neointimal hyperplasia more effectively. The biochemical assays further reveal that the enhanced restenosis prevention effect is contributed to the selective release of RAPA at the injured sites of artery, which notably potentiate the nanosystem as a systemically targeting delivered treatment.

KEYWORDS: *Thermo/pH-Response, Anti-Collagen IV Peptide, Fe_3O_4@Nanogels, Rapamycin, Restenosis.*

INTRODUCTION

Coronary artery disease (CAD) threatens numerous human lives around the world.[1] An important clinical procedure for CAD is percutaneous coronary intervention (PCI).[2] However, up to 50% of PCI-treated patients suffer from vascular restenosis, a common complication of PCI, and the unpredictable procedural outcomes are the major drawback of PCI.[3] Restenosis is a result of arterial damage during interventional therapy and over-reaction of vascular endothelial injury. The pathological process of restenosis includes local inflammation caused by vascular endothelial injury, secondary hyperplasia and migration of vascular smooth muscle cells, followed by neointimal proliferation, which accelerates the formation of vascular restenosis.[4]

Some antiproliferative pharmacological agents, such as paclitaxel (PTX) and rapamycin (RAPA), are FDA-approved drugs for preventing or treating vascular

---

*Authors to whom correspondence should be addressed.
Emails: yoyoyoung8293@gmail.com, anderson-qian@163.com
Received: 9 February 2018
Accepted: 22 March 2018

restenosis via systemic delivery. However, because of the intrinsic hydrophobic features of these drugs, their bioavailability and therapeutic outcome remain unsatisfactory, which cause a series of adverse effects.[5] Although drug-eluting stents (DES) with cytotoxic or cytostatic drug coatings have been developed to reduce the percentage of restenosis and indeed have good therapeutic effects for coronary artery stenosis, nonspecific drugs diffusing on the vascular tissue lead to delayed reendothelialization around the stented area, and the resulting in-stent restenosis (ISR) and late stent thrombosis (LST) impose further limitations on the long-term clinical outcome.[6] Therefore, efficient strategies for site-specific delivery of therapeutic agents are needed.

The pathological process and the microenvironment of restenosis may provide some promising targets for specific delivery of therapeutic agents. A variety of ligands have been explored for active targeting delivery of antiproliferative drugs. In particular, collagen type IV exists abundantly at the basal lamina of the artery wall, which is exposed after endothelial denudation by after endovascular device implants.[7–9] Collagen type IV is a promising target for drug delivery during restenosis evolution. Furthermore, collagen type IV-targeting peptides are efficient ligands for injured vessel targeting.[10, 11] Thus, modification with collagen type IV-targeting peptides may enhance the delivery efficacy of antiproliferative drugs.

As a new type of drug delivery system, nanoparticle-based delivery systems with adjustable properties are offering promising new approaches for the diagnosis and therapy of many diseases, including cancers, immunological and cardiovascular diseases.[12, 13] Compared with the traditional approaches, nano-drug delivery systems possess unique physical and biochemical advantages, which can significantly improve the biodistribution of drugs while minimizing the adverse effects due to their controllable release characteristics and targeting properties.[14–16] Among the various nano-drug delivery systems, nanogels are soft nano-sized networks composed of hydrophilic or amphiphilic polymer chains that give high-stability, smart responses to environmental stimuli (temperature, pH and bio-catalysis), and they are easily functionalizable.[17–19] They exhibit great potential as drug delivery carriers, including small-molecule delivery, biomacromolecule delivery, and even small nanoparticle delivery.[20]

In our previous work, we have developed thermal/pH dual-responsive nanogels for delivery of cisplatin with controllable release behavior.[21] Because of the existence of thermal-responsive groups (*N*-isopropylacrylamide (NIPAm), lower critical solution temperature (LCST) is 32 °C), the nanogels showed simulative deformability of swelling-shrinkage, and the hydrophobic drug can also be encapsulated and stabilized (self-assembling) by nanogels at physiological temperature (37 °C).[22] However, without the targeting ligands, the delivery efficacy still needs to be improved. The acid-triggered shrinkage properties may also attenuate the drug release because the endosome and lysosome are acidic.

Therefore, in this study, based on our previous research, we constructed antiproliferative drug-loaded nanogels that could specifically target collagen type IV and enhance the drug release in acidic environment. RAPA was chosen as the model antiproliferative drug. NIPAm was still used as a thermo-responsive monomer, and *N*-isopropylmethacrylamide (NIPMAm) was used to control the LCST of the nanogels.[23] Poly(ethylene glycol) methacrylate (PEGMA) was used to enhance the hydrophilicity of the nanogels to enhance the stability, which is critical during peptide modification. 2-Aminoethyl methacrylate hydrochloride (AEMA) units were also introduced into the structure of the nanogels. It not only protonates in the intracellular environment and enhances drug release by nanogel swelling but also can conjugate with ligands to facilitate the targeting nanogel system.[24] A peptide (KLWVLPK) was used as the ligand to target to collagen type IV. To provide the nanogels with imaging functions, magnetic nanoparticles (MPS-grafted Fe_3O_4 NPs) were introduced into the nanogel structure. The hydrophobic surface of magnetic nanoparticles may also favor enhanced loading of hydrophobic drugs.[25, 26] Then, we established a rat carotid artery model of balloon angioplasty and administered RAPA-loaded nanogels to evaluate the therapeutic effect of the nanogels constructed in this work. *In vitro* and *in vivo* experiments demonstrated that the RAPA-loaded targeting nanogels prevented vascular restenosis efficiently and did not induce inflammation or architectural changes in arteries or organs.

MATERIALS AND METHODS

Materials

N-isopropylacrylamide (NIPAm), *N*-isopropylmethacrylamide (NIPMAm), poly(ethylene glycol)methacrylate (PEGMA, Mn 360), 2-Aminoethyl methacrylate hydro chloride (AEMA), Potassium persulfate (KPS), *N*,*N*-methylene bis(acrylamide) (MBA), 3-(Trimethoxysilyl) propyl methacrylate (MPS), cetyltrimethylammonium bromide (CTAB), 4-(*N*-Maleimidomethyl) cyclohexanecarboxylic acid *N*-hydroxysuccinimide ester(sulfo-SMCC), methyl thiazolyl tetrazolium (MTT), were purchased from Sigma-Aldrich (USA). 2,2′-azobis[2-methyl-*N*-(2-hydroxyethyl) propionamide] (VA-086) was provided from Wako Chemicals Gmbh. The peptide segments (KLWVLPKGGGC) was synthesized by GL Biochem (Shanghai, China) LTD. Rapamycin (RAPA, MW: 914.17) was obtained from Dalian Meilun Biotechnology, CO., LTD. The cell counting kit (CCK-8), Rat interleukin-1β (IL-1β) and tumor necrosis factor-α (TNF-α) ELISA kits were from R&D Systems (USA). Dulbecco's Modified Eagle Medium (DMEM), antibiotic/antimycotic solution, and fetal bovine serum were purchased from Gibco

(Thermo Fisher Scientific, USA). Anti-PCNA (ab15497), Anti-Ki67 (ab15580) and Anti-CD31(ab28364) antibody for immunohistochemistry, inducible nitric oxide synthase (iNOS), endothelial nitric oxide synthase (eNOS), and β-actin antibodies used in western blot were purchased from Abcam (USA) and CST (USA), respectively. All other solvents and reagents used in this study were commercially available with analytical reagent grade.

Cell Lines

A7r5 cell lines (thoracic aorta smooth muscle cell) and HUVEC used in this study were purchased from American Type Culture Collection (ATCC, Rockville, MD), which were grown in DMEM medium supplemented with 10% of FBS, 1% of penicillin/streptomycin, respectively. The cell cultures were maintained in a 37 °C incubator with humidified 5% of CO_2 atmosphere.

Animals

All the animals (Male Sprague Dawley rats, 12–16 weeks old) were all purchased from Dasuo Bioscience Co. Ltd., China and kept under SPF condition with free access to standard food and water. All animal care and experimental protocols were performed in compliance with Guide for the Care and Use of Laboratory Animals in Chengdu Medical College.

Construction of RAPA-Loaded Targeting Nanogels

Synthesis of Fe_3O_4@Nanogels (Fe_3O_4@NGs)

MPS-grafted Fe_3O_4 NPs were prepared according to the previous reports.[27] Briefly, Fe_3O_4 NPs were first synthesized according to the method introduced by Liu et al.[28, 29] The obtained Fe_3O_4 NPs were then dispersed in ethanol and deionized water and then added to 3-(trimethoxysilyl) propyl methacrylate (MPS) for another 48 h of stirring. The MPS-grafted Fe_3O_4 NPs were washed and dried overnight for further use.

In a typical synthesis, 1 g of a NIPAm, NIPMAm, AEMA, and PEGMA mixture (the composition of the comonomers is listed in Table I) plus 5 mol% total monomers of MBA were dissolved in 85 mL of DI water that contained 40 mg of CTAB as a surfactant. The mixture was degassed for 15 min, followed by adding a 10 mg suspension of MPS-grafted Fe_3O_4 NPs with mechanical stirring, and then it was heated to 40 °C. After 1 h stirring, the mixture was heated to 70 °C and stirred vigorously with N_2 backfilling until the temperature remained stable.[30] A solution of the desired concentrations of VA-086 and APS was injected into the flask to initiate polymerization for 2 h.[31] Following the synthesis, a degassed solution of AEMA (10 mL) was added in 1 h (where appropriate) by LongerPump, and the polymerization proceeded for another 1 h. The products were dialyzed for 5 days until the monomers and surfactant were removed, and then they were collected by magnetic adsorption.

Table I. **The optimization of the nanogels synthesis.**[a]

	NIPAm (%)	NIPMAm (%)	PEGMA (%)	AEMA (%)	Transition temperature (°C)	Yield (%)
1	84	0	6	10	32.6	85.3
2	47	37	6	10	34.1	84.5
3	39	45	6	10	35.4	86.5
4	32	52	6	10	40.8	77.4

Note: [a]Each sample also contains 5 mol% MBA as a cross-linker.

Preparation of RAPA-Loaded Nanogels (RAPA/Fe_3O_4@NGs)

Twenty milligrams of the purified Fe_3O_4@NGs was pre-iced for 10 min, and then 500 μL of 36.8 μM RAPA ethanol solution was added dropwise. The solution was vortexed vigorously for 10 min, followed by gentle stirring at 0 °C for 1 h, and then slowly warmed to room temperature. After that, the ethanol in the solution was evaporated at 37 °C for another 2 h. The obtained RAPA/Fe_3O_4@NGs were separated by an Amicon Ultra-4 centrifugal filter with 30 kDa MWCO (Millipore) and washed with 0.01 M phosphate-buffered saline (PBS, pH 7.4) three times. Drug-loading content (DLC) and entrapment efficiency (EE) were calculated according to the following respective formulas:

$$\text{DLC}\ (\%) = (W_{\text{encapsulated RAPA}}/W_{\text{NGs}}) \times 100$$

$$\text{EE}\ (\%) = (W_{\text{encapsulated RAPA}}/W_{\text{total RAPA}}) \times 100$$

where W_{NGs} is the weight of the RAPA/Fe_3O_4@NGs after lyophilization and $W_{\text{encapsulated RAPA}}$ and $W_{\text{total RAPA}}$ are the weights of RAPA detected in the lyophilized RAPA/Fe_3O_4@NGs and of initial RAPA, respectively.

The amount of encapsulated RAPA in the drug-loaded NGs was measured by a reversed-phase high-performance liquid chromatography (HPLC) system. To extract RAPA from RAPA/Fe_3O_4@NGs, 5 mg of lyophilized samples was dissolved in 1 mL acetonitrile. Then, 9 mL of methanol was added to precipitate the polymers. After being centrifuged at 15,000 rpm for 10 min, the supernatant was separated and dried under nitrogen stream. The drug concentration was analyzed by an Agilent 1260 HPLC system with a C18 column (4.6 mm × 150 mm, 5 μm, Agilent, US). The mobile phase was methanol/water (80/20, v%) with a flow rate of 1 mL/min. The column temperature was 35 °C, and the sample concentrations were measured at 278 nm. All measurements were taken in triplicate.

Construction of Anti-Col IV Peptide–Conjugated NGs (Fe_3O_4@NGs-Col IV) and RAPA-Loaded Fe_3O_4@NGs-Col IV (RAPA/Fe_3O_4@NGs-Col IV)

Fe_3O_4@NGs or RAPA-loaded Fe_3O_4@NGs (10 mg/mL) were incubated in 0.1 M PBS (pH 7.2) for 1 h at room temperature in the presence of sulfo-SMCC (with final concentration of 2 mg/mL). The anti-Col IV peptides (at a 1/2 molar ratio to sulfo-SMCC) were previously reduced using disulfide bond-breaker DTT solution (in 2 mM PBS-EDTA) and then incubated with activated NGs overnight in the dark at room temperature. After that, the final products were washed three times using an Ultra-4 centrifugal filter with 30 kDa MWCO to remove the excess crosslinking reagents and free peptides.

Physicochemical Characterization of Nanogels (NGs)

^{1}H-Nuclear Magnetic Resonance Analysis (^{1}H-NMR)

^{1}H NMR spectra (in D_2O) were recorded on a Varian 400 spectrometer (Varian, USA) at 400 MHz using tetramethylsilane as an internal reference standard.

Fourier Transform Infrared Spectroscopy (FT-IR)

The surface chemistry of the lyophilized Fe_3O_4@NGs was evaluated using FT-IR analyses on a Nicolet 6700 FTIR spectrometer (Thermo Scientific). Transmission infrared spectra were obtained in the wavenumber range of 400–4000 cm^{-1}.

Morphology

The morphological and structural information of NGs was measured by a field-emission high-resolution transmission electron microscope (HRTEM, Tecnai G2 F20 S-TWIN, FEI, American), operating at an acceleration voltage of 100 kV. The samples were prepared by dropping them on 400-mesh carbon-coated copper grid. The excessive solvent was immediately evaporated for negative staining of samples, followed by staining with phosphotungstic acid (1%) and drying at room temperature.

Size Distribution

The hydrodynamic particle sizes, polydispersity index (PdI) and zeta potentials of NGs were determined using a Zetasizer instruments (Zetasizer nano ZS, Malvern, British) at 25 °C. The measurements were performed with Milli-Q water and different pH buffers at a NG concentration of 30 μg/mL. The hydrodynamic diameters of the NGs at various temperatures (from 15 °C to 55 °C) and various pH values (between 4 and 8.5) were characterized by measuring the hydrodynamic diameter (D_h) variation. The diameter-temperature/pH values curves were fitted with the Boltzmann function.

In Vitro Drug Release of the RAPA/Fe_3O_4@NGs-Col IV

In vitro release experiments were also carried out at room and physiological temperature. RAPA/Fe_3O_4@NGs-Col IV (5 mg) were re-dispersed in 2 mL PBS (0.01 M, pH = 7.4), then placed in a dialysis bag with a molecular weight cutoff of 7 kDa. They were dialyzed against 30 mL of releasing medium at 37 °C with gentle shaking (90 rpm). At predetermined time points, the releasing medium was collected and replaced by fresh medium. The collected samples were analyzed to determine the concentration of RAPA by HPLC as described above. Both pH 7.4 and 5.8 PBS buffer (0.2 M, contained 0.5% of Tween-80 at 37 °C) were chosen to investigate the influence of pH on RAPA release.

MRI Signal Enhancement of Fe_3O_4@NGs-Col IV *In Vitro*

The MRI signals of the Fe_3O_4@NGs-Col IV in aqueous solution were measured by an Animal MRI instrument (BioSpec70/20USR, Bruker). To test the contrast ability of the magnetic nanogels, the Fe_3O_4@NGs-Col IV dispersions at various concentrations of Fe (quantitatively determined by TGA) were evaluated. Water was used as a control. The magnetic field strength was 7 T, and the turbo RARE sequence for was used for T_2-weighted imaging.

Cytotoxicity Assay of Fe_3O_4@NGs-Col IV

Cytotoxicity of the Nanocarriers

To evaluate the cytotoxicity of Fe_3O_4@NGs-Col IV (denoted as the carrier), HUVECs and A7r5 cells were seeded in 96-well plates at a density of 5000 cells per well in 100 μL of DMEM. After 24 h preincubation, the culture medium was replaced by 200 μL of fresh medium containing gradient concentrations of Fe_3O_4@NGs-Col IV, and the cells were incubated for another 24 h. The cell viability was quantified by the MTT assay.

Cellular Accumulation of Fe_3O_4@NGs-Col IV

A7r5 cells were seeded in 6-well plates at a density of 2×10^5 cells per well, preincubated in DMEM medium for 24 h, and incubated with C6 loaded-Fe_3O_4@NGs-Col IV (10 μg/mL C6 concentration). At the designed time points, the cells were washed with PBS and then labeled with 5 μg/mL DAPI at 37 °C for 20 min. The cells were fixed with 4% paraformaldehyde and visualized by fluorescence microscopy (Zeiss OBSERVER D1/AX10 cam HRC). Further quantification of cellular uptake was conducted by flow cytometry. After incubation with C6 loaded-Fe_3O_4@NGs-Col IV for various durations, a certain number of cells were washed by PBS and then collected for flow-cytometric analysis (NovoCyte™ Flow Cytometer, ACEA Bioscience. Inc., USA).

In Vitro Anti-Proliferative Activity in A7r5 SMCs Cells

A7r5 cells were cultured in a 96-well plate (5000 cells per well) with DMEM for 24 h. After the medium was changed to one containing 0.5% FBS, PDGF-BB at 20 ng/mL was added, concomitant with various concentrations of blank Fe_3O_4@NGs-Col IV, free RAPA and RAPA/Fe_3O_4@NGs-Col IV. Cells in the control group were treated with PDGF-BB growth medium alone. After

24 or 48 h of incubation, the cell viability was determined by using a cell counting kit (CCK-8).

Targeting Affinity in an Angioplasty Model of Injured Artery

The rat carotid artery balloon injury model was prepared as described.[32] Briefly, male Sprague-Dawley rats (450–500 g) were anesthetized by i.p. injection of pentobarbital sodium (80 mg/kg) and additionally given heparin (500 IU/kg) by i.v. injection before surgery. Then, a segment of the left carotid artery was exposed to create an arteriotomy incision. A 2 F Fogarty balloon catheter (Edwards Life sciences) was inserted to injure the artery by repeatedly advancing, inflating, and withdrawing the balloon to induce endothelial cell loss and mural distension.

To study the targeting affinity, we used Cy5 fluorescent dye as a substitute for drug loading to visualize the Fe_3O_4@NGs optical imaging.[33] The *in vitro* fluorescence intensities of dye-loaded NGs dispersions with various concentrations were measured in a 96-well plate using the IVIS Lumina XR system (excitation = 645 nm, emission = 715 nm long pass). After the angioplasty procedure, 2 mL of dye-encapsulated Fe_3O_4@NGs or Fe_3O_4@NGs-Col IV was i.v. administered (at approximately 25 μg/mL of Cy5). Twelve hours post-injection, the rats were sacrificed, and the injured left carotid arteries as well as the normal right carotid arteries were harvested and subjected to *ex vivo* fluorescence imaging with the IVIS Lumina XR system by using the same parameters described above.

Treatment of Rat Carotid Artery Balloon Injury by Different RAPA Formulations

Twenty Sprague-Dawley rats were randomly divided into five groups ($n = 4$): a normal control group, a sham injury-only group, and treated groups administered with free RAPA, RAPA/Fe_3O_4@NGs, and RAPA/Fe_3O_4@NGs-Col IV, respectively. Angioplasty models of injured artery were established in other rats according to the above procedures, excluding rats in the normal control group. After angioplasty, different samples were i.v. administered at 1 mg/kg of RAPA, and an equal i.v. dose was repeatedly given another 3 times at 5-day intervals. On the 21st day after angioplasty, all the rats were euthanized. The carotids and major organs were excised for further histological evaluation, immunohistochemistry, and western blot analysis.

Histological Analysis

The formalin-fixed tissues were embedded in paraffin and sectioned. The sliced tissues were stained with hematoxylin and eosin (H&E) and observed by Zeiss microscope under the bright-field setting.

ImageJ software was used to measure the thickness of neointimal (N) and medial (M) areas in arteries. The averages from 3 sections were taken. The degree of neointimal hyperplasia was expressed as the N/M ratio, and the highest N/M ratio representing the site of greatest narrowing was assigned to each artery.

Immunohistochemistry

These histological sections of carotids were also stained with antibodies against proliferating cell nuclear antigen (PCNA) and Ki67 to measure proliferation and against CD31 for endothelial cell staining. Antibodies used for immunohistochemistry were purchased from Abcam (USA).

Measurement of Interleukin-1β(IL-1β) and Tumor Necrosis Factor-α(TNF-α)

When the rats were killed, blood samples were collected and centrifuged immediately at 7,000 rpm for 10 min at 4 °C. Then, serum samples were separated and stored at −80 °C for further analysis. The levels of TNF-α and IL-1β were analyzed by enzyme-linked immunosorbent assay kits (R&D Systems, USA).

Western Blot Analysis

Frozen arteries were homogenized with lysis buffer (0.5 M Tris-HCl, pH 7.4, 1.50 M NaCl, 25% deoxycholic acid, 10% NP-40, 10 mM EDTA) and centrifuged at 14,000 rpm at 4 °C for 20 min. Supernatants were used as whole-cell lysates, and protein concentration was determined using the BCA method. Extracted proteins from tissues (80 μg) were resolved by 10% SDS-PAGE. Proteins were then electro transferred onto PVDF membranes at 120 V for 1 h. After blocking in 5% nonfat powdered milk for 1 h, the membranes were washed and treated with antibodies against iNOS, eNOS and anti β-actin (1:1,000) overnight at 4 °C. After washing, the membranes were incubated with HRP-conjugated secondary antibody IgG (1:5,000) for 1 h at room temperature. After washing, bands were visualized with ECL (Bio-Rad, USA), quantified by densitometry (Bio-Rad) and analyzed by ImageJ software. The normalization protein was β-actin. Antibodies used in western blotting were purchased from CST (USA).

Statistical Analysis

A statistical analysis was performed using SPSS 15.0 software (IBM corporation, Armonk, NY). The results of multiple group comparisons are all indicated as the mean ± standard derivations and were analyzed using a one-way analysis of variance (ANOVA). $p < 0.05$ was considered statistically significant.

RESULTS AND DISCUSSION

Construction and Characterization of Fe_3O_4@NGs

The magnetic Fe_3O_4 NPs were prepared by co-precipitation and coated with OA, then MPS was used to modify the surface of nanoparticles with methacrylate

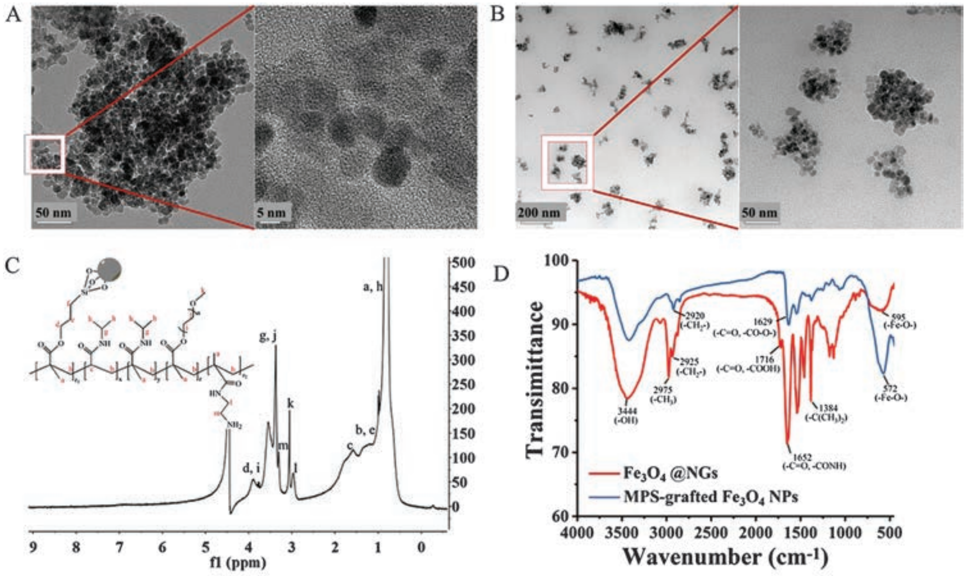

Figure 1. **Characterization of the Fe_3O_4@NGs. (A) HRTEM images of Fe_3O_4 NPs. (B) HRTEM images of Fe_3O_4@NGs. (C) ^{1}H-NMR spectra of Fe_3O_4@NGs. (D) FTIR spectra of Fe_3O_4 NPs (blue), and Fe_3O_4@NGs (red).**

groups. TEM images (Fig. 1(A)) showed that Fe_3O_4 NPs were uniform spheres with diameters of approximately 8 to 10 nm, which easily aggregated because of their magnetic property.

The core–shell Fe_3O_4@NGs were composed of MPS-grafted Fe_3O_4 NPs, NIPAm, NIPMAm, PEGMA, AEMA, and MBA as the cross-linker, as illustrated in Scheme 1. TEM imaging of the obtained NGs without negative staining showed Fe_3O_4 NPs separated into stable clusters, which indicated that the polymers formed the outer shell structure of NGs and made the magnetic Fe_3O_4 nanoparticles separate from their original state (Fig. 1(B)).

^{1}H-NMR and FT-IR analyses were performed to further confirmed the chemical composition of Fe_3O_4@NGs. The correspondent chemical shifts and vibration peaks of the NIPAm, NIPMAm, PEGMA, AEMA and unsaturated bonds were identified from the ^{1}H-NMR and FT-IR spectra, respectively. From the ^{1}H-NMR spectra (Fig. 1(C)), no unreacted vinyl peaks from the nanogels were observed in the range of 5.5–6.5 ppm. Based on the integrated peak areas of the $(CH_3)_2CH–$ protons ($\delta g \approx 0.9$ and 3.4 ppm) from NIPAm and NIPMAm, the $CH_3–O–$ protons ($\delta g \approx 3.1$ ppm) and the $–CH_2–CH_2–O–C{=}O$ protons ($\delta g \approx 3.4$ and 3.8 ppm) from PEGMA, and the $NH_2–CH_2–CH_2–NH–$ protons ($\delta g \approx 2.9$ and 3.3 ppm) from AEMA, we confirmed that these co-monomers were all introduced into the molecular structure of the nanogels. This was further confirmed by the FT-IR characterization. Compared with that of MPS-grafted Fe_3O_4 NPs, the FT-IR spectrum of Fe_3O_4@NGs possessed some characteristic peak absorbance bands of monomers (Fig. 1(D)). The bands at 2975 cm^{-1} and 2925 cm^{-1} were attributed to stretching vibrations of $–CH_3$ and $–CH_2$ from AEMA, respectively. The strong absorbance bands at 1652 cm^{-1} and 1352 cm^{-1} were assigned to the –CO–NH– and $–CH(CH_3)_2$ groups from NIPAm/NIPMAm, respectively. Furthermore, the band at 572 cm^{-1} was due to the Fe–O bond of magnetite. These data demonstrate that these monomers were successfully grafted on the surface of Fe_3O_4 NPs.[34, 35]

From our previous report, the introduction of PEG segments enhanced the stability of NG suspension because of the enhancement of their hydrophilicity.[34] The introduction of amine monomer AEMA gave the NGs additional functionality.[36] With the PEGMA and AEMA molar contents fixed, the phase-transition temperature of NGs shifted from ~32.4 °C to ~41.2 °C by changing the feeding ratio of NIPAm to NIPMAm (Table I). For Fe_3O_4@NG synthesis, the co-monomer ratio used in the following discussion was settled as sample 3, with the LCST of approximately 35 °C (Table II). These data suggest that the NGs could display a state of dehydration at 37 °C and maintained amphiphilic properties for drug loading. However, when MPS-grafted Fe_3O_4 NPs were introduced, the NG1, synthesized using 5% VA-086 as the initiator, precipitated in water resulted in low yield and inhomogeneous particle size (Fig. 2(A-I)), while using 1% APS (NG3) as the initiator led to over polymerization and instability in the aqueous phase. The NG2 and NG4, synthesized with 4.8% VA-086 plus 0.2% APS as the initiator, were more stable. The negative-staining TEM image of NG2 demonstrated that the black center denoted the Fe_3O_4 nanoparticles as the core, while the clear polymeric layer around the center was a shell, and the surfaces of the particles were smooth (Fig. 2(A-II)). Nevertheless, by increasing the amount of Fe_3O_4 NPs in the initial solutions, a mixture of uniform spherical and anomalous nanogels was formed (NG4, Fig. 2(A-III)).

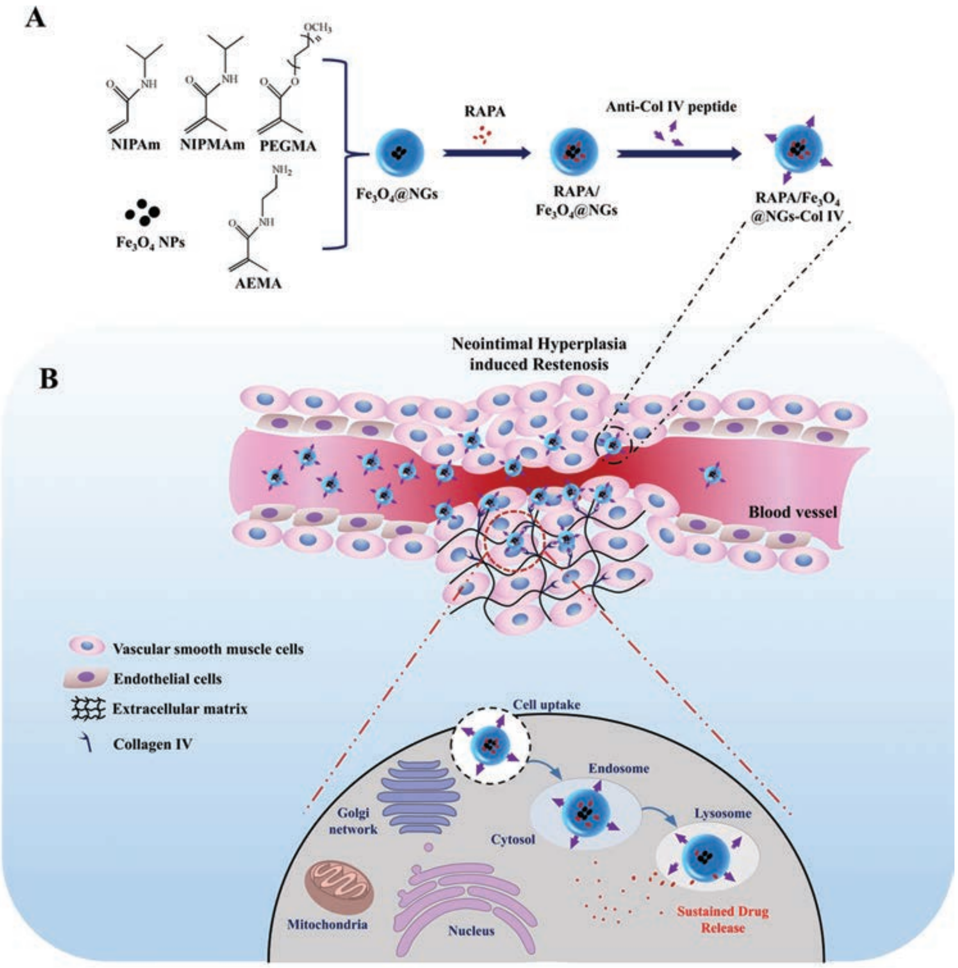

Scheme 1. **Schematic illustration of targeting therapy for vascular restonsis by the RAPA-loaded thermo/PH responsive Fe_3O_4@nanogels. (A) The construction of RAPA/Fe_3O_4@NGs-Col IV, (B) RAPA/Fe_3O_4@NGs-Col IV exerts long circulation time after intravenous administration, and also presents targeting properties binding to the collagen IV, which forms the matrix of the basal lamina in the artery wall and guarantee the enrichment of RAPA at the injury site. After internalization, RAPA/ Fe_3O_4@NGs-Col IV shows sustained releases of RAPA in the cytoplasm, resulting in enhanced inhibition of neointimal hyperplasia and promissing MRI imaging ability.**

Surface Conjugation with the Anti-Collagen Peptide on Fe_3O_4@NGs and RAPA-Loaded Fe_3O_4@NGs

The primary amine groups of Fe_3O_4@NGs were first activated with the heterobifunctional linker sulfo-SMCC to introduce reactive maleimide groups for covalently conjugating with anti-Col IV peptide (KLWVLPK) via a C-terminal GGGC linker.[37] From the HR-TEM imaging, the obtained Fe_3O_4@NGs-Col IV still maintained typical spheres of a core–shell architecture and homogeneous distribution, similar to that of Fe_3O_4@NGs (Figs. 2(A-IV and A-V)).

Table II. **The composition of the magnetic nanogels synthesized in this study.[a]**

	NIPAm[b] (%)	NIPMAm[b] (%)	PEGMA[b] (%)	AEMA[b] (%)	Fe_3O_4 NPs (mg)	Initiator	Yield (%)	Particles size (25 °C)
NG1	39	45	6	10	50	5.0% VA-086	44.5%	212.3 ± 28.7 nm
NG2	39	45	6	10	50	4.8% VA-086 0.2% APS	86.5%	205.4 ± 6.2 nm
NG3	39	45	6	10	50	1% APS	NA	NA
NG4	39	45	6	10	100	4.8% VA-086 0.2% APS	77.4%	226.1 ± 8.7 nm

Notes: [a]Each sample also contains 5 mol% MBA as a cross-linker. [b]The total monomer weight of each sample is settled at 1 g.

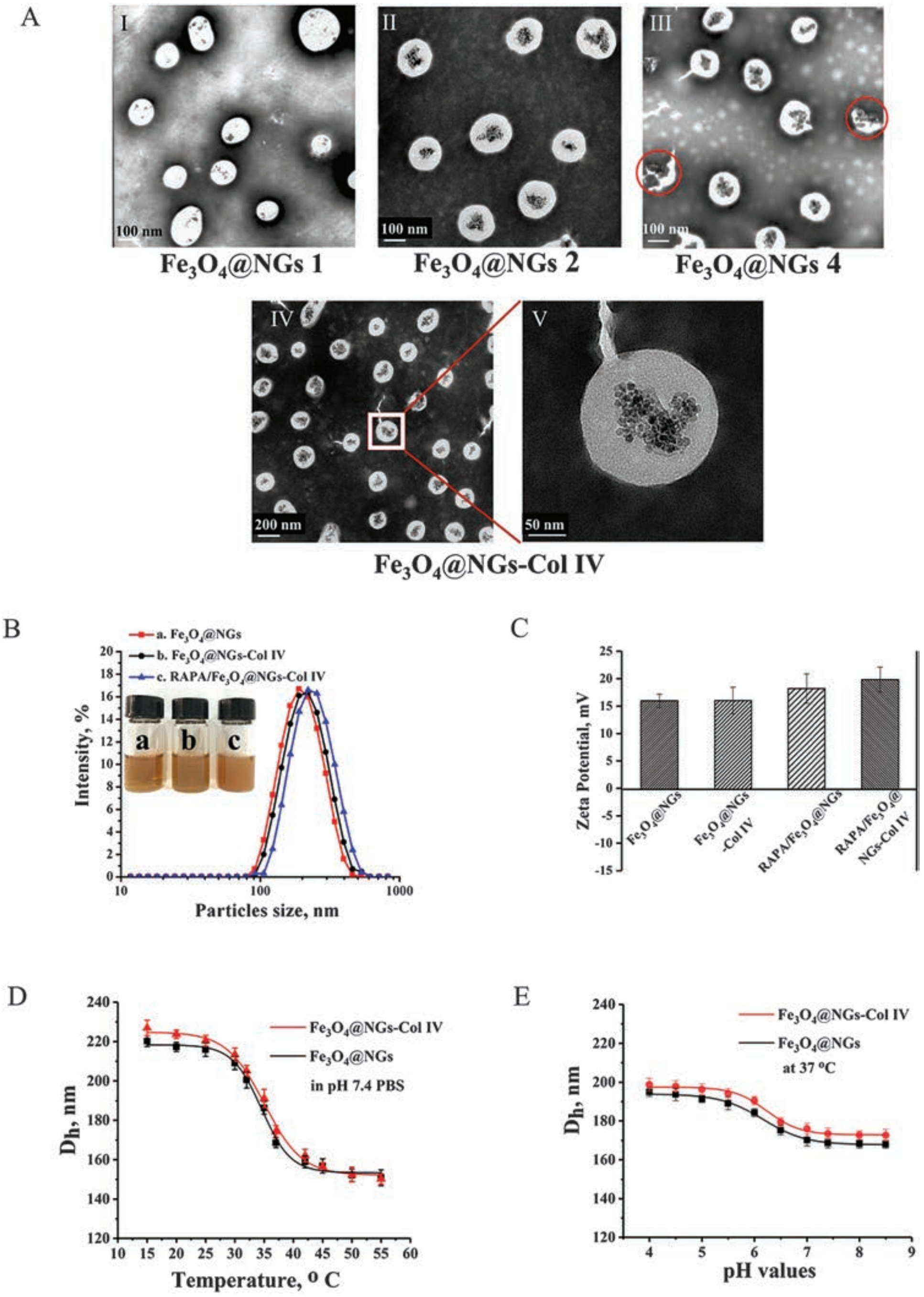

Figure 2. (A) TEM images of Fe_3O_4@NGs 1, 2, 4 and HRTEM image of Fe_3O_4@NGs-Col IV. All the samples were negatively stained with 1% phosphotungstic acid before imaging. (B and C) Hydrodynamic size distribution and zeta potential of the correspond samples, respectively. (D) Hydrodynamic size of the Fe_3O_4@NGs and Fe_3O_4@NGs-Col IV and in PBS (pH 7.4) buffer. (E) Hydrodynamic size distribution of Fe_3O_4@NGs and Fe_3O_4@NGs-Col IV in different pH solution.

As shown in Figure 2(B), the hydrodynamic particles size of Fe_3O_4@NGs-Col IV was approximately 226 nm, slightly larger than the Fe_3O_4@NGs (220 nm). The same phenomenon was observed when loading with the anti-proliferation drug RAPA (the RAPA/Fe_3O_4@NGs and RAPA/Fe_3O_4@NGs-Col IV had diameters of approximately 215 nm and 243 nm, respectively). The size distributions of different NGs were narrow, reflected by the small polydispersity (PDI) (<0.15). Nevertheless, the surface charges of Fe_3O_4@NGs, Fe_3O_4@NGs-Col, RAPA/Fe_3O_4@NGs and RAPA/Fe_3O_4@NGs-Col IV were +15.97, +16.01, +18.20, and +19.84 mV, respectively. These results show that the peptide-conjugated NGs were slightly more positive than the NGs without conjugation, presumably due to the cationic surface charge from the exposed *N*-terminal anti-Col IV peptide (Fig. 2(C)).

For vascular targeting, the particle size is a critical parameter for the distribution in the arterial wall.[38, 39] As shown in Figure 2(D), both Fe_3O_4@NGs and Fe_3O_4@NGs-Col IV were markedly shrunken at 37 °C. The average particle size of Fe_3O_4@NGs-Col IV decreased from 215.9 ± 2.7 nm to 156.8 ± 2.1 nm as the temperature increased from 25 °C to 45 °C, which was attributed to the hydrophobic transition of NIPAm and NIPMAm groups. Meanwhile, a weak pH-responsiveness of these NGs was observed in the pH range of 4.0–8.5 (Fig. 2(E)). These NGs were nearly 25 nm larger in diameter at pH 5.5 than that at pH 7.4, which was due to the electrostatic repulsion between the protonated primary amine groups of AEMA moieties. These results suggest that the thermal contraction property might give the NGs a long circulation capacity and prevent the burst release of hydrophobic drugs in systemic circulation. Furthermore, the NGs will slightly swell when in an endosomal-like acidic environment (pH 5.5), which favors controlled drug release.

Drug Loading and *In Vitro* Release of RAPA/Fe_3O_4@NGs-Col IV

Drug loading and release are important parameters for drug efficacy. At a temperature above the LCST of NGs (37 °C), the polymeric shell became dehydrated, which allowed the NGs to shrink in aqueous solution.[22] The shrinkage property of Fe_3O_4@NGs-Col IV enabled the hydrophobic drug RAPA to be entrapped in the gel network. The RAPA-loading capacity of NGs reached 3.86%, and the loading efficiency reached 55% by adjusting the RAPA content. In the following experiments, RAPA/Fe_3O_4@NGs and RAPA/Fe_3O_4@NGs-Col IV with the DLC of 3.75% were used, whose contents detected by HPLC were 3.86% and 3.63%, respectively.

We evaluated the release behavior of RAPA/Fe_3O_4@NGs-Col IV in the simulated physiological condition (pH 7.4) and an acidic environment (pH 5.8) at 37 °C to assess the feasibility of controlled release. The accumulated release of RAPA was almost 60% in 48 h when at room temperature (25 °C). In contrast, only 30% of the total drug was released from RAPA/Fe_3O_4@NGs-Col IV in the extracellular environment (pH 7.4, 37 °C). These results indicate that the diffusion of RAPA from the shrunken NG network was rather slow. Additionally, pH gradients can control the drug release of RAPA/Fe_3O_4@NGs-Col IV. When the pH approached that of endosomes (pH 5.8), the accumulated release of RAPA was almost 50% in the first 24 h, followed by sustained release in the next 4 days. During this period, 80.2% of the drug was released (Fig. 3(A)). More interestingly, when we investigated the cumulative amount of RAPA release by using media with pH values of 7.4 and 5.8, approximately 30% of RAPA was released in the initial 48 h at pH 7.4, and more than 86% of drug was released in the same time period at pH 5.8 (Fig. 3(B)). The enhanced RAPA release triggered by lower pH was attributed to the swelling of NGs by the protonation of the amino groups in the acidic environment. Furthermore, the increased temperature may have enhanced the solubility and diffusion of RAPA. Therefore, the drug release from the designed NGs could be accelerated when in the cytoplasm.

In Vitro MR Imaging of the Nanosystem

To evaluate the MR imaging performance of the Fe_3O_4@NGs-Col IV, the transverse relaxation time (T_2) of the nanogel dispersion was measured at 7.0 T with an Animal MRI instrument.[40] The representative T_2-weighted MR images of the magnetic nanogels are shown in Figure 4(A). With an increased concentration of Fe in Fe_3O_4@NGs-Col IV dispersions, an obvious darkening of T_2-weighted MRI was observed. The transversal relaxivity (r_2), which was evaluated via linear least-square fitting of $1/T_2$ (s^{-1}) versus iron concentration (mM Fe), was calculated to be 186.17 mM^{-1} S^{-1} (Fig. 4(B)). The enhancement in T_2 sensitivity can be ascribed to the synergistic effect of clustered magnetic nanoparticles within the inner core of nanogels, which gives Fe_3O_4@NGs-Col IV the potential for application as MRI contrast agents.[41, 42]

In Vitro Cytotoxicity of Fe_3O_4@NGs-Col IV and RAPA-Loaded Fe_3O_4@NGs-Col IV

Before their application to vascular smooth muscular cells (VSMCs), the cellular uptake of Fe_3O_4@NGs-Col IV was measured. The A7r5 cells treated with Fe_3O_4@NGs-Col IV showed gradual fluorescence signal enhancement as the incubation time increased. The merge images showed that majority of the NGs were localized in the cytoplasm. In addition, the intracellular fluorescence intensity of C6 in Figure 5(A) demonstrated that Fe_3O_4@NGs-Col IV accumulated in the cytoplasm of the A7r5 cells. The uptake efficiency depended on incubation time, which was also confirmed by the flow cytometry after incubation for 8 h (Figs. 5(B and C)). All these results indicate that the nano-sized Fe_3O_4@NGs-Col IV had relative effectiveness as therapeutic cargoes for intravascular drug delivery strategies.

The biocompatibilities of Fe_3O_4@NGs-Col IV nanocarriers were investigated by their cytotoxic effects on HUVECs and A7r5 cells. As shown in Figure 6(A), the viabilities of HUVECs and A7r5 cells in the presence of high concentrations of Fe_3O_4@NGs-Col IV with were all above 85%, indicating that the nanocarriers were suitable for biomedical applications.

Since rapamycin inhibits SMC proliferation, we further investigated the anti-proliferative activity of various RAPA formulations. Treatment by PDGF-BB alone induced considerable proliferation of A7r5 cells (Figs. 6(B and C)), while incubation with 900 ng/mL free RAPA decreased the PDGF-BB-induced proliferation from 92.8% to 52.9%

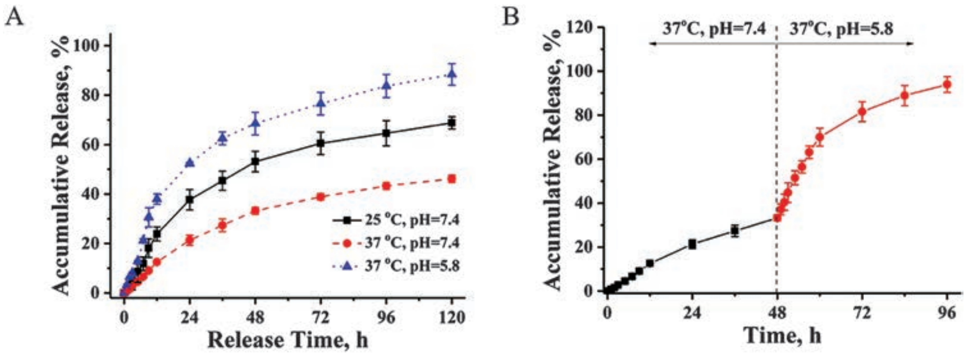

Figure 3. (A) *In vitro* drug release profiles of RAPA from RAPA/Fe_3O_4@NGs-Col IV in PBS at different pH value and different temperature. (B) Drug release profiles of RAPA/Fe_3O_4@NGs-Col IV in PBS buffer with pH 7.4 and 5.8 respectively, at 37 °C.

at 24 h and 41.1% at 48 h. Compared with free RAPA, the same dose of RAPA/Fe_3O_4@NGs-Col IV had a significantly increased inhibition effect on A7r5 cell proliferation. According to the drug release profiles *in vitro*, a faster drug release occurred when the drug-loaded NGs internalized into the cells from the physiologic environment, resulting in a desirable pH-triggered drug release in the cytoplasm and a further anti-proliferation effect.

Targeting Affinity of Fe_3O_4@NGs-Col IV at the Injured Carotid Arteries

Next, we evaluated the targeting affinity of the Fe_3O_4@NGs-Col IV nanosystem at the injury site of the carotid artery. The Cy5-loaded Fe_3O_4@NGs-Col IV (with average diameter of 223.5 ± 4.3 nm) were used for further *ex vivo* targeting affinity measurement, and the *in vitro* fluorescence imaging was also evaluated. The results showed that the fluorescence intensities increased with increasing concentration of Cy5 in the range of 2.5–40 μg/mL (Fig. 7(A)).

After the angioplasty procedure, Cy5/Fe_3O_4@NGs or Cy5/Fe_3O_4@NGs-Col IV were intravenously injected. *Ex vivo* imaging of the carotid artery isolated at 12 h after administration clearly illuminated the localization of Fe_3O_4@NGs-Col IV at the injured site of the left balloon-injured carotid artery (Fig. 7(B)). Fe_3O_4@NGs-Col IV obviously accumulated at the injury site of left artery compared with that of the right artery without injury. By contrast, with non-targeting administration of Cy5, weak fluorescence intensities were observed at both the injured and normal arteries (Fig. 7(C)). These results show that the Fe_3O_4@NGs-Col IV had better efficiency of injury site enrichment than the Fe_3O_4@NGs did. Therefore, the anti-Col IV conjugated NGs were chosen as an ideal drug delivery platform in the further *in vivo* anti-restenosis experiments.

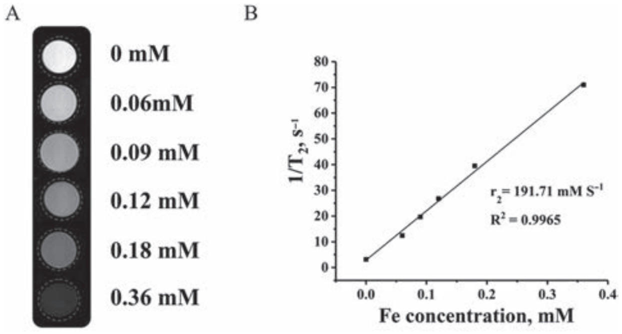

Figure 4. (A) *In vitro* T_2-weighted MR images of Fe_3O_4@NGs-Col IV at different concentrations measured with a 7.0 T MRI. (B) T_2-weighted molecular relativity (r_2) of Fe_3O_4@NGs-Col IV calculated from the MR images.

Targeted Treatment of Restenosis by Different RAPA Formulations

Based on the above promising results, *in vivo* anti-restenosis experiments were conducted to examine the therapeutic benefits of different RAPA treatments in the injured carotid artery of rats. After induction of the arterial endothelial injury, different RAPA formulations were administered intravenously in different groups. At day 21, rats were euthanized, and the injured carotid artery segments were isolated for microscopic study. At the same time, the main organs were harvested for histological analysis (Fig. 8(A)).

Figure 8(B) shows representative H&E-stained histological sections of carotid arteries excised from rats with the different treatments. Compared with the normal control, significant neointimal hyperplasia was observed in the sham group (injury only). All the examined RAPA formulations showed relatively attenuated restenosis of carotid arteries compared to that of the sham, injury-only group. Consistent with this observation, we found notably reduced neointimal area in RAPA formulation–treated rats, while no significant changes occurred in the medial area. The artery neointima-to-media ratio (N/M ratio) was used to evaluate the degree of neointimal hyperplasia (Fig. 8(C)).[11] The sham group (injury only) exhibited the highest N/M ratio, while significantly reduced N/M ratios were observed in all RAPA treatment groups. Moderately, intravenous treatment with free RAPA considerably decreased neointimal thickness compared to that

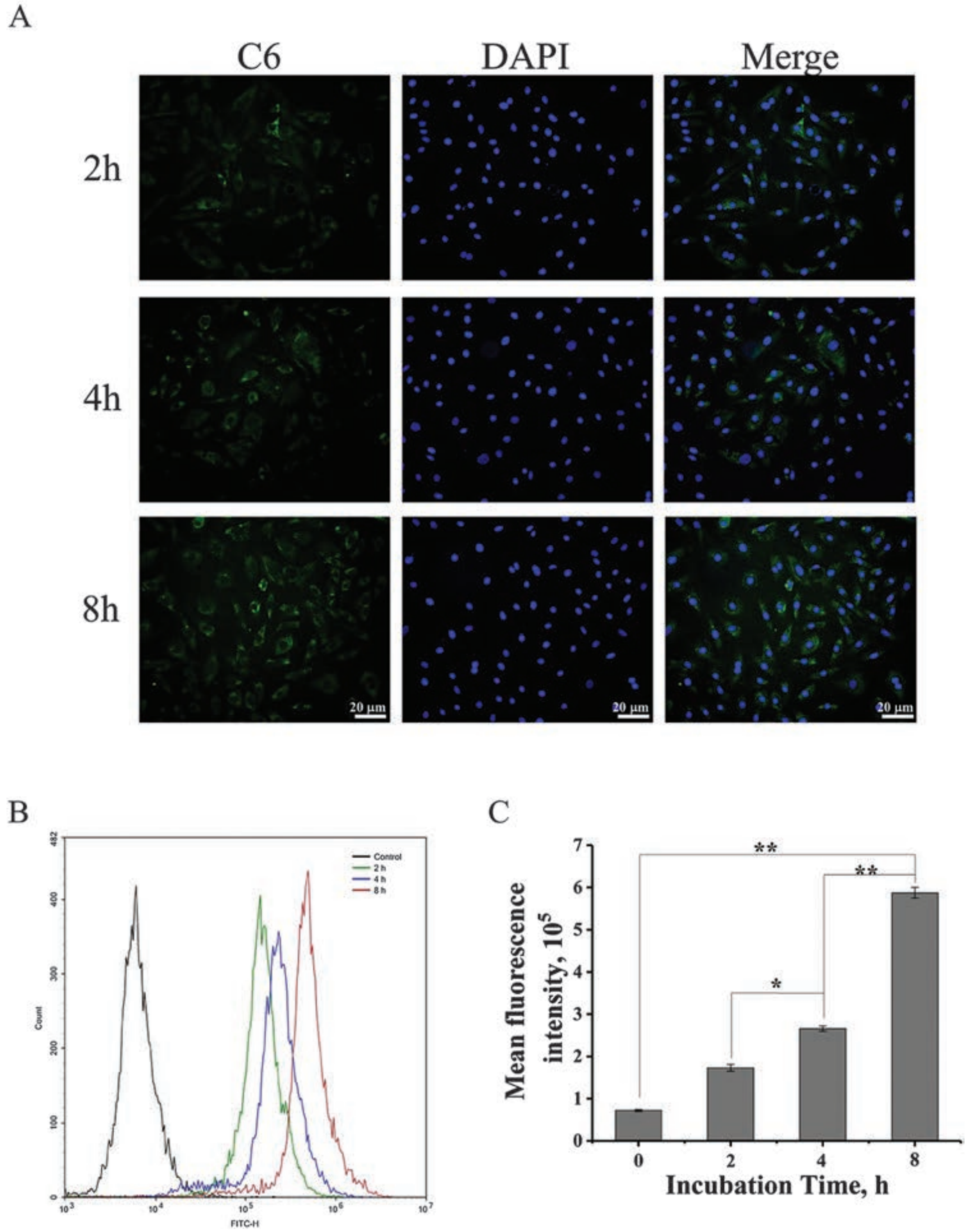

Figure 5. **(A) Fluorescence images of A7r5 smooth muscle cells after being incubated with C6-loaded Fe_3O_4@NGs-Col IV for 2, 4 and 8 h, cell nuclei were stained with DAPI. The scale bar is 20 μm. (B) Flow cytometric histogram profiles of A7r5 cells incubated with C6-loaded Fe_3O_4@NGs-Col IV at 37 °C. (C) Flow cytometry expressed as geometric mean fluorescence intensity. Data represents standard deviations (SD) of determination ($n = 3$ each) ("∗" $P < 0.05$, "∗∗" $P < 0.01$ vs. control).**

of the sham group, and the most significant therapeutic effect was realized after either RAPA/Fe_3O_4@NGs or RAPA/Fe_3O_4@NGs-Col IV administration. Most importantly, treatment with Fe_3O_4@NGs-Col IV showed the lowest N/M ratio ($N/M = 0.41 \pm 0.032$). The quantitative analysis demonstrated that the anti-Col IV peptide—based RAPA targeted delivery markedly reduced neointimal hyperplasia of the carotid artery after balloon injury.

Further evaluations of the therapeutic effect on vascular restenosis were performed by immunohistochemistry. As an important biological indicator of injury-induced neointima hyperplasia, the proliferation of responding SMC cells in the neointima was examined by PCNA and Ki67 staining.[43, 44] Artery sections from the sham (injury-only) group had many PCNA- and Ki67-positive cells, while the free RAPA–treated group showed slightly decreased PCNA- and Ki67-positive staining in the neointima. Likewise, a significant reduction of positive cells was observed in the RAPA/Fe_3O_4@NGs-Col IV treatment group (Figs. 9(A and B)).

Immunohistochemical staining for CD31 represents the re-endothelialization of the arteries, which is the one of most important therapeutic factors for inhibiting restenosis.[45] The endothelial cell layer was clearly

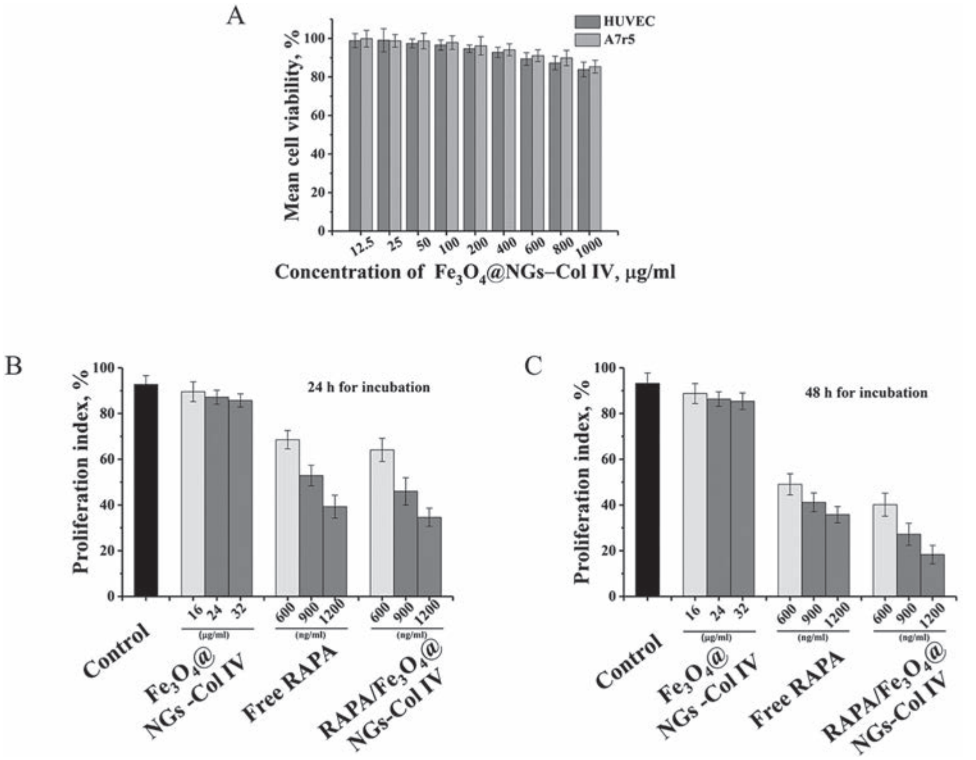

Figure 6. (A) Cytotoxicity of Fe_3O_4@NGs-Col IV to A7r5 smooth muscle cells and HUVEC cell lines. (B and C) *In vitro* inhibition effects of free RAPA and RAPA/Fe_3O_4@NGs-Col IV on proliferation of A7r5 smooth muscle cells, for 24 and 48 h, respectively. Data represents standard deviations (SD) of determination ($n = 6$ each).

aligned around the normal artery luminal surface, while no CD31 staining was observed within the neointima, of the sham injury-only group. However, CD31-positive endothelial cell (EC) coverage was hardly observed at the neointimal surface in the free RAPA–treated group. RAPA/Fe_3O_4@NG-treated groups showed a lower proportional CD31-positive area, while the neointimal surface was nearly completely covered with positive ECs in

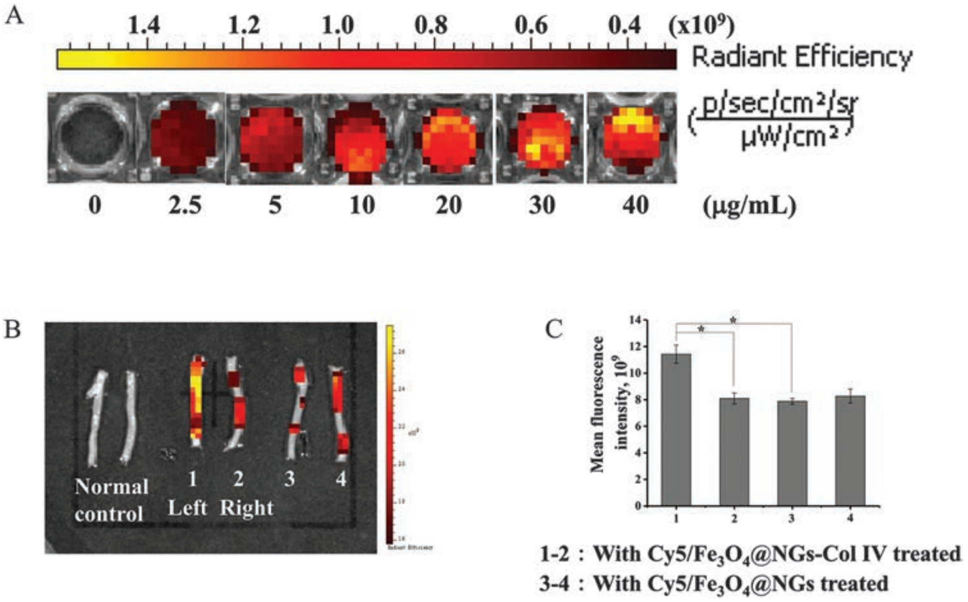

Figure 7. *In vivo* systemic deliveries in a carotid angioplasty model. For imaging, Cy5 dye were encapsulated in place of RAPA drug loading. (A) NIR fluorescence images of collected carotid arteries after 4 h i.v. of saline, Cy5/Fe_3O_4@NGs-Col IV and Cy5/Fe_3O_4@NGs, respectively. (B) NIR fluorescence intensities of carotid arteries lesion by different administrations ($n = 3$, "$*$" $p < 0.05$ vs. control).

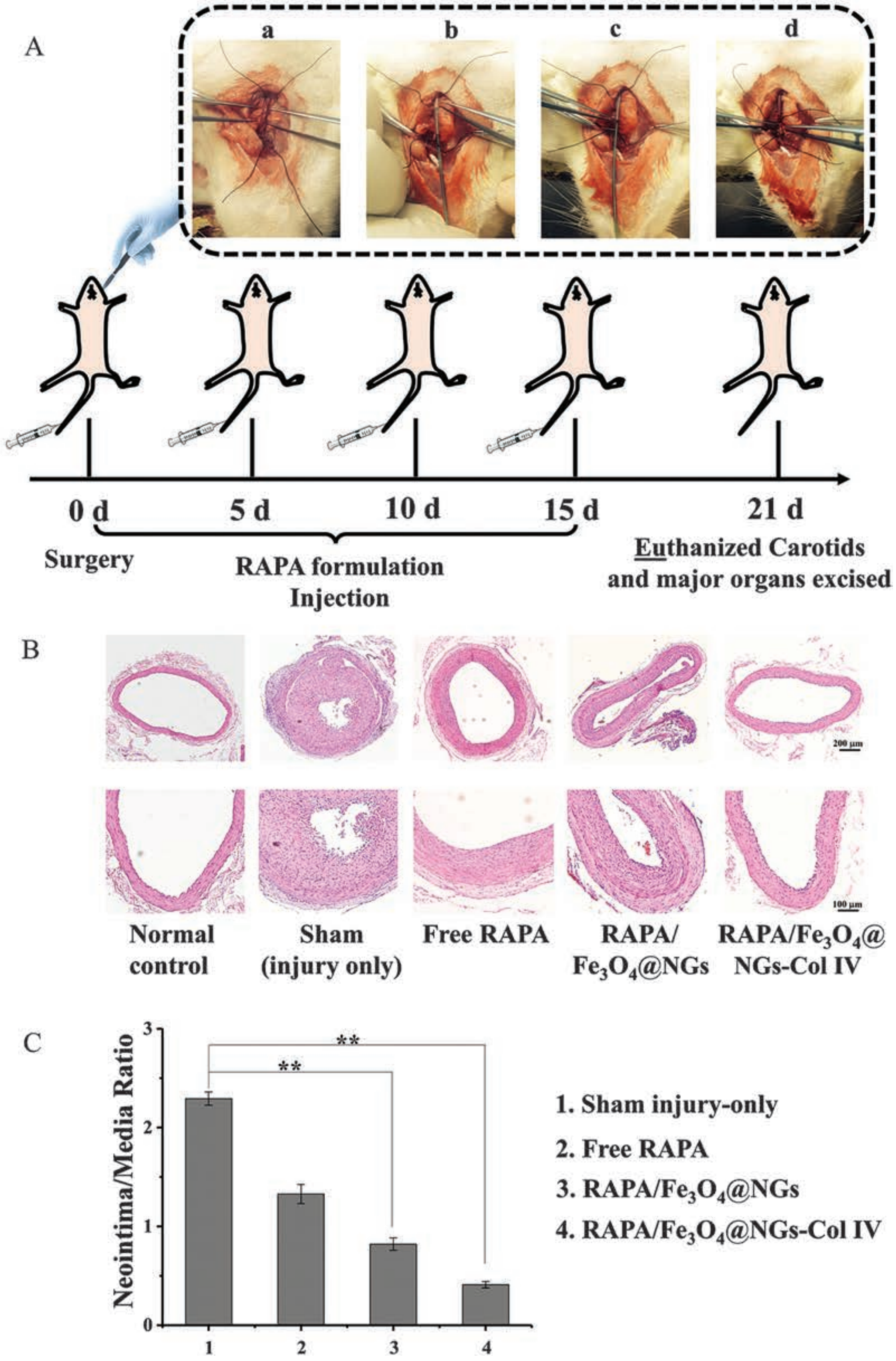

Figure 8. (A) Schematic illustration of the administration route of RAPA formulations in a carotid angioplasty model. Process of surgery: (a) Left carotid artery exposition and arteriotomy, (b) balloon catheter inserted, (c) artery injury, (d) reperfusion. After angioplasty in rats, different RAPA formulations were i.v. administered at 1 mg/kg of RAPA on day 0, 5, 10, and 15. The carotid arteries were isolated at day 21 for subsequent analyses. (B) H&E stained histological sections of carotid arteries isolated from rats subjected to various treatments. Scale bars were 200 μm (the upper panel), and 100 μm (the lower panel). (C) Quantitative analysis on neointima/media ratio of carotid arteries from rats with different treatments. Statistical difference between groups ("$**$" $P < 0.01$ vs. control).

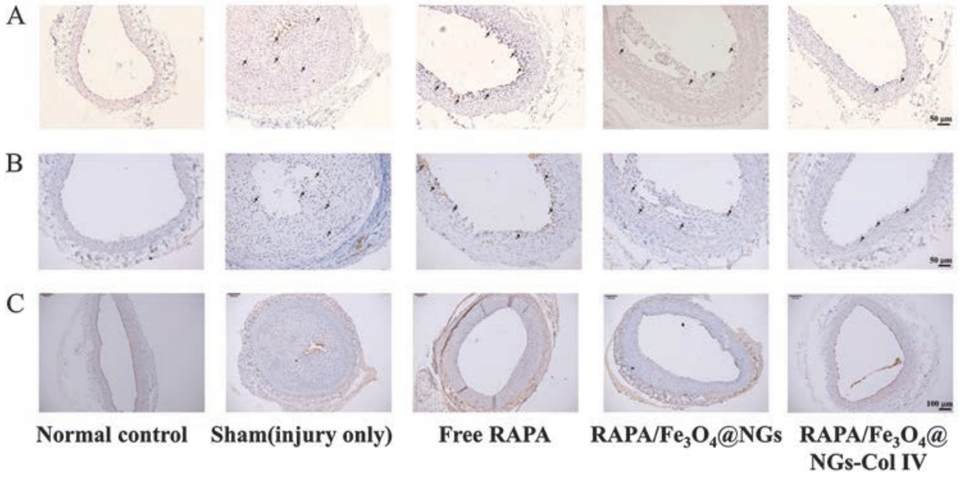

Figure 9. Representative the PCNA (A) and Ki-67 (B) immunohistochemical staining for different treatments in effects on intimal hyperplasia in balloon-injured rat carotid arteries, respectively. The arrow points to PCNA and Ki67 positive cells (stained brown) (Scale bar = 50 μm). (C) Reendothelialization expressed as CD31 immunohistochemical staining of injured artery after treatment with different formulations. (Scale bar = 100 μm).

the RAPA/Fe_3O_4@NGs-Col IV–treated group. These findings indicate significant therapeutic effects of inhibiting neointimal proliferation and promoting reendothelialization (Fig. 9(C)).

Histological analysis was performed on the main organs, including the heart, liver, kidney and spleen, after the therapeutic treatment (Fig. 10). No tissue toxicity or visible differences were found with a therapeutic dose of RAPA/Fe_3O_4@NGs-Col IV compared to the normal control rats.

ELISA Assay for Serum Level of Inflammatory Markers

Since the inflammatory response of endothelial denudation results in neointimal hyperplasia by vascular damage, the inhibition of the inflammation at injured vascular sites has become a recent focus in preventing restenosis.[4, 46] Inflammatory cytokines, including TNF-α and IL-1β, might indirectly affect SMC activation and proliferation, subsequently inducing neointimal hyperplasia. Importantly, the anti-inflammatory property of RAPA plays a role in

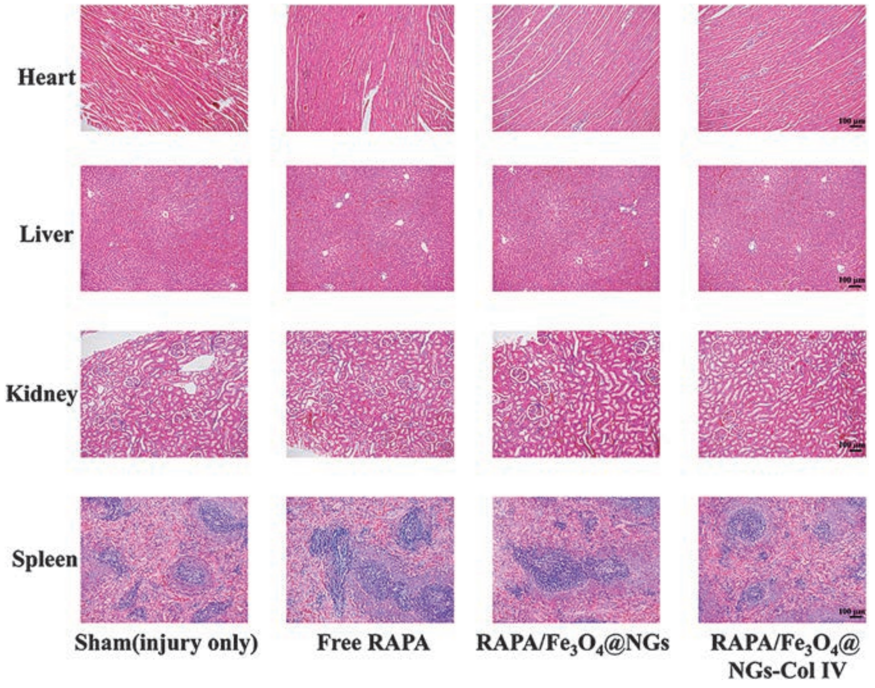

Figure 10. Histological characterization of the heart, liver, kidney and spleen tissues obtained from rats of different treatment groups (Scale bar = 100 μm).

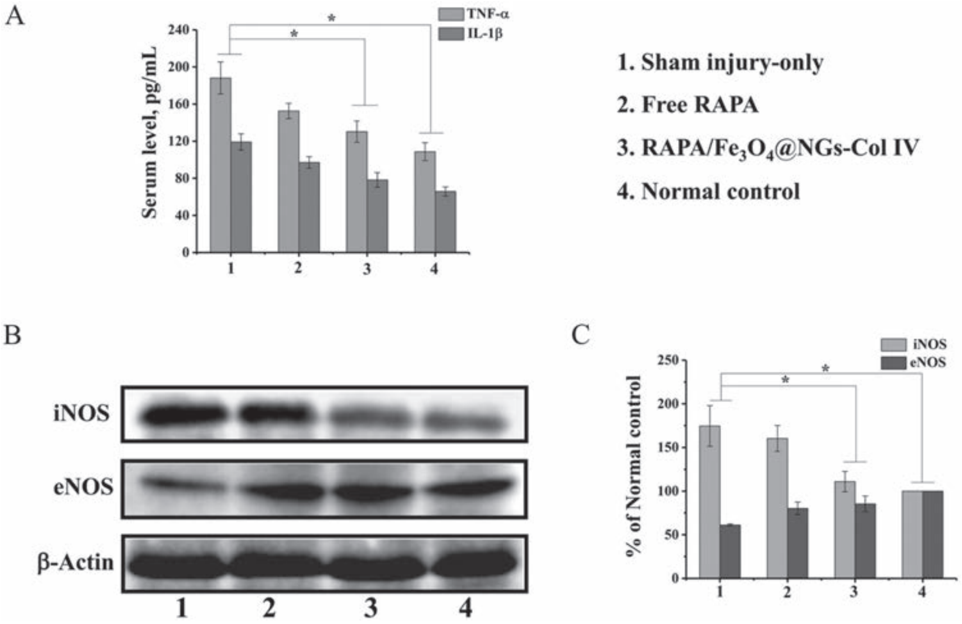

Figure 11. (A) Representative the serum level of TNF-α and IL-1β at 21 days after the balloon angioplasty. (B) Representative western blot for iNOS and eNOS detection after artery injury. (C) Graph of combined data for iNOS and eNOS protein levels. ("$*$" $P < 0.05$ vs. sham).

preventing neointimal hyperplasia.[47] Accordingly, serum TNF-α and IL-1β were determined in rats with different treatments by ELISA (Fig. 11(A)). The increased TNF-α and IL-1β in serum of the balloon angioplasty-injured group was associated with an inflammatory response, while after systemic RAPA administration, the slightly decreased TNF-α and IL-1β reflected attenuation of inflammatory vascular injury. The local targeting RAPA-loaded NGs for restenosis showed a visible suppression of TNF-α and IL-1β compared with the injury-only group, indicating significant anti-inflammatory activities.

Western Blot for Tissue Detection

Following vascular injury, damaged endothelial cells and activated SMCs cause decreased eNOS activity and arginine-dependent NO generation.[48] The NO generated by eNOS provides vascular protection, such as vasorelaxation, control of leukocyte adherence, an inhibition of SMC proliferation and migration, which play important roles in regulating intimal hyperplasia after arterial injury.[49] Increased expression of iNOS within the hyperplastic intima after vascular injury suggests a compensatory mechanism in response to injured endothelium and decreased eNOS expression.[50] In the sham (injury-only) group, the arterial endothelial injury led to increased expression of the iNOS protein (193.2%), whereas eNOS protein expression decreased (33.6%), compared to the normal control rat vascular tissue, indicating endothelial injury and a VSMC proliferation response. The free RAPA–treated group had decreased iNOS protein. Similarly, the RAPA/Fe_3O_4@NGs-Col IV–treated group had reduced iNOS band intensity and enhancement of eNOS protein expression compared to the sham group, which indicated a protective effect against arterial endothelial injury in the form of reendothelialization (Figs. 11(B and C)).

In agreement with the serum levels of inflammatory markers, the targeting RAPA-loaded NG administration demonstrated better vascular reendothelialization and effectively suppressed the anti-inflammatory response, suggesting the inhibition of neointimal-hyperplastic vascular restenosis without delaying endothelial healing.

CONCLUSIONS

In this study, we developed temperature- and pH-responsive nanogels with a magnetic inner core as a multifunctional nanoplatform for drug delivery and MRI/fluorescence imaging. The thermo-/pH-responsive nanogels achieved controlled intracellular release of RAPA and significantly reduced the adverse effects of RAPA. More importantly, the multiple primary amino groups on the particle surface allow for conjugation with targeting ligands under mild conditions. Since collagen type IV forms the matrix of the basal lamina in the artery wall, which are simply exposed after balloon angioplasty, the presence of the anti-collagen IV peptide on the surface of nanogels makes Fe_3O_4@NGs-Col IV ideal candidates for the enhancement of targeting efficiency in drug delivery.

Meanwhile, the magnetic Fe_3O_4 inner core showed enhanced T_2-weighted MRI resolution, providing a high potential for imaging-guided therapy. The *ex vivo* targeting investigation showed the efficacy of the nanogel platform for injured vessel wall binding. The *in vivo* findings showed the significant reductions of the N/M ratio and proliferation of SMC cells in neointima by RAPA/Fe_3O_4@NGs-Col IV administration following balloon injury. In addition to their beneficial inhibitory effects, we further demonstrated the therapeutic performance of Col IV-targeted nanogels for systemic delivery of rapamycin: they inhibited restenosis without delaying endothelial healing, which was identified by ELISA and western blot. Our findings indicate that the Fe_3O_4@NGs-Col IV nanosystem may have potential benefits as a systemically targeting delivery mechanism for injured vasculature, replacing stent placement, to prevent restenosis.

ASSOCIATED CONTENT

Author Contributions

The manuscript was written through contributions of all authors. All authors have given approval to the definitive version of the manuscript.

Funding Sources

This work was financially supported by the National Natural Science Funds of China (NSFC31600811, NSFC31771096, and NSFC31500809), the National Natural Science Fund of China for Distinguished Young Scholar (NSFC31525009), the Application Fundamental Research Foundation of Sichuan Province Science and Technology Department, China (Grant No. 2016JY0157), the International Science and Technology Cooperation Program of Sichuan Province, China (Grant No. 2013HH0054), the Scientific Research Foundation of the Health and Family Planning Commission of Sichuan Province, China (Grant No. 17PJ556).

Declaration of Interest

The authors declare no competing financial interest.

Acknowledgment: We thank Dr. Tao Fu from West China School of Preclinical and Forensic Medicine and Dr. Shanling Wang from Analytical and Testing center, Sichuan University, P. R. China for the TEM observation and analysis of the data.

REFERENCES

1. D. S. Celermajer, C. K. Chow, E. Marijon, N. M. Anstey, and K. S. Woo, Cardiovascular disease in the developing world. *J. Am. Coll. Cardiol.* 60, 1207 (**2012**).
2. R. A. Byrne, G. W. Stone, J. Ormiston, and A. Kastrati, Coronary balloon angioplasty, stents, and scaffolds. *The Lancet* 390, 781 (**2017**).
3. J. W. Jukema, J. J. Verschuren, T. A. Ahmed, and P. H. Quax, Restenosis after PCI. Part 1: Pathophysiology and risk factors. *Nat. Rev. Cardiol.* 9, 53 (**2012**).
4. J. E. Tengood, I. Fishbein, R. J. Levy, and M. Chorny, Nanomedicines for restenosis therapy, Handbook of Nanobiomedical Research Fundamentals, Applications and Recent Developments: Applications in Therapy, World Scientific, Singapore (**2014**), Vol. 2. pp. 39–87.
5. I. Fishbein, M. Chorny, and G. Golomb, Treatment of restenosis by controlled-delivery systems of tyrphostins. *Drug Develop. Res.* 50, 487 (**2000**).
6. J. W. Jukema, T. A. Ahmed, J. J. Verschuren, and P. H. Quax, Restenosis after PCI. Part 2: Prevention and therapy. *Nat. Rev. Cardiol* 9, 79 (**2012**).
7. O. McLeod, P. Dunér, A. Samnegård, P. Tornvall, J. Nilsson, A. Hamsten, and E. Bengtsson, Autoantibodies against basement membrane collagen type IV are associated with myocardial infarction. *Int. J. Cardiol. Heart Vasc.* 6, 42 (**2015**).
8. M. Osidak, E. Osidak, M. Akhmanova, S. Domogatsky, and A. Domogatskaya, Fibrillar, fibril-associated and basement membrane collagens of the arterial wall: Architecture, elasticity and remodeling under stress. *Curr. Pharm. Des.* 21, 1124 (**2015**).
9. P. Dunér, I. Gonçalves, H. Grufman, A. Edsfeldt, F. To, M. Nitulescu, J. Nilsson, and E. Bengtsson, Increased aldehyde-modification of collagen type IV in symptomatic plaques—A possible cause of endothelial dysfunction. *Atherosclerosis* 240, 26 (**2015**).
10. E. S. Bahnson, H. A. Kassam, T. J. Moyer, W. Jiang, C. E. Morgan, J. M. Vercammen, Q. Jiang, M. E. Flynn, S. I. Stupp, and M. R. Kibbe, Targeted nitric oxide delivery by supramolecular nanofibers for the prevention of restenosis after arterial injury. *Antioxid. Redox Signal.* 24, 401 (**2016**).
11. J. M. Chan, J.-W. Rhee, C. L. Drum, R. T. Bronson, G. Golomb, R. Langer, and O. C. Farokhzad, *In vivo* prevention of arterial restenosis with paclitaxel-encapsulated targeted lipid–polymeric nanoparticles. *Proc. Natl. Acad. Sci. USA* 108, 19347 (**2011**).
12. G. Chen, I. Roy, C. Yang, and P. N. Prasad, Nanochemistry and nanomedicine for nanoparticle-based diagnostics and therapy. *Chem. Rev.* 116, 2826 (**2016**).
13. K. Zhang, P.-P. Yang, J.-P. Zhang, L. Wang, and H. Wang, Recent advances of transformable nanoparticles for theranostics. *Chin. Chem. Lett.* 28, 1808 (**2017**).
14. N. Kamaly, B. Yameen, J. Wu, and O. C. Farokhzad, Degradable controlled-release polymers and polymeric nanoparticles: Mechanisms of controlling drug release. *Chem. Rev.* 116, 2602 (**2016**).
15. Y. Li, J. Sun, Q. Chen, Z. Chen, and L. Zhu, Fast drug release of liposome-gold conjugation under light irradiation and the comparison with liposome-gold hybrid. *Nanosci. Nanotechnol. Lett.* 9, 982 (**2017**).
16. E. Ren, J. Wang, and G. Liu, Cell-surface cascaded landing location for nanotheranostics. *Chin. Chem. Lett.* 28, 1799 (**2017**).
17. P. Ji, B. Zhou, Y. Zhan, Y. Wang, Y. Zhang, Y. Li, and P. He, Multistimulative nanogels with enhanced thermosensitivity for intracellular therapeutic delivery. *ACS Appl. Mater. Interfaces* 9, 39143 (**2017**).
18. Z. Cao, X. Zhou, and G. Wang, Selective release of hydrophobic and hydrophilic cargos from multi-stimuli-responsive nanogels. *ACS Appl. Mater. Interfaces* 8, 28888 (**2016**).
19. L. Yu, Y. Chen, and H. Chen, H_2O_2-responsive theranostic nanomedicine. *Chin. Chem. Lett.* 28, 1841 (**2017**).
20. A. J. Sivaram, P. Rajitha, S. Maya, R. Jayakumar, and M. Sabitha, Nanogels for delivery, imaging and therapy. *Wiley Interdiscip. Rev. Nanomed. Nanobiotechnol.* 7, 509 (**2015**).
21. J. Peng, T. Qi, J. Liao, B. Chu, Q. Yang, W. Li, Y. Qu, F. Luo, and Z. Qian, Controlled release of cisplatin from pH-thermal dual responsive nanogels. *Biomaterials* 34, 8726 (**2013**).
22. H. Chen, H. Zhu, J. Hu, Y. Zhao, Q. Wang, J. Wan, Y. Yang, H. Xu, and X. Yang, Highly compressed assembly of deformable nanogels into nanoscale suprastructures and their application in nanomedicine. *ACS Nano* 5, 2671 (**2011**).
23. T. Hoare, B. P. Timko, J. Santamaria, G. F. Goya, S. Irusta, S. Lau, C. F. Stefanescu, D. Lin, R. Langer, and D. S. Kohane, Magnetically triggered nanocomposite membranes: A versatile platform for triggered drug release. *Nano Lett.* 11, 1395 (**2011**).

24. M. Pernia Leal, A. Torti, A. Riedinger, R. La Fleur, D. Petti, R. Cingolani, R. Bertacco, and T. Pellegrino, Controlled release of doxorubicin loaded within magnetic thermo-responsive nanocarriers under magnetic and thermal actuation in a microfluidic channel. *ACS Nano* 6, 10535 (**2012**).

25. J. Hu, A. Dehsorkhi, W. T. Al-Jamal, Y. Zhang, S. Chen, C. Yang, D. Tan, Q. Zhao, C. Yang, and Y. Wang, Studies on the photothermal effect of PEGylated Fe_3O_4 nanoparticles. *Nanosci. Nanotechnol. Lett.* 9, 556 (**2017**).

26. K. Zhu, Z. Zhu, H. Zhou, J. Zhang, and S. Liu, Precisely installing gold nanoparticles at the core/shell interface of micellar assemblies of triblock copolymers. *Chin. Chem. Lett.* 28, 1276 (**2017**).

27. B. Liu, C. Bai, D. Zhao, W.-L. Liu, M.-M. Ren, Q.-Z. Liu, Z.-Z. Yang, X.-Q. Wang, and X.-L. Duan, Novel ferroferric oxide/polystyrene/silver core–shell magnetic nanocomposite microspheres as regenerable substrates for surface-enhanced Raman scattering. *Appl. Surface Sci.* 364, 628 (**2016**).

28. X. Wang, H. Liu, D. Chen, X. Meng, T. Liu, C. Fu, N. Hao, Y. Zhang, X. Wu, and J. Ren, Multifunctional Fe_3O_4@P(St/MAA)@Chitosan@Au core/shell nanoparticles for dual imaging and photothermal therapy. *ACS Appl. Mater. Interfaces* 5, 4966 (**2013**).

29. Z. Abbasi, S. Rezayati, M. Bagheri, and R. Hajinasiri, Preparation of a novel, efficient, and recyclable magnetic catalyst, γ-Fe_2O_3@HAp-Ag nanoparticles, and a solvent- and halogen-free protocol for the synthesis of coumarin derivatives. *Chin. Chem. Lett.* 28, 75 (**2017**).

30. L.-L. Li, R.-Y. Jiang, J.-X. Chen, M.-Z. Wang, and X.-W. Ge, One-step synthesis of self-healable hydrogels by the spontaneous phase separation of linear multi-block copolymers during the emulsion copolymerization. *Chin. Chem. Lett.* 28, 868 (**2017**).

31. P. Huo, J. Li, Z. Ye, H. Wang, X. Liu, X. Li, and Y. Yan, Fabricated temperature sensitive photocatalyst of PNIPAM@ZnO/C for controllable photocatalytic activity. *Chin. Chem. Lett.* 28, 2259 (**2017**).

32. D. A. Tulis, In rat carotid artery balloon injury model, Vascular Biology Protocols, Methods in Molecular Medicine™, edited by N. Sreejayan and J. Ren, Humana Press, New York City (**2007**), Vol. 139, pp. 1–30.

33. H. Gao, Progress and perspectives on targeting nanoparticles for brain drug delivery. *Acta Pharmaceutica Sinica B* 6, 268 (**2016**).

34. J. Peng, T. Qi, J. Liao, M. Fan, F. Luo, H. Li, and Z. Qian, Synthesis and characterization of novel dual-responsive nanogels and their application as drug delivery systems. *Nanoscale* 4, 2694 (**2012**).

35. B. Du, A. Mei, P. Tao, B. Zhao, Z. Cao, J. Nie, J. Xu, and Z. Fan, Poly[*N*-isopropylacrylamide-co-3-(trimethoxysilyl)-propylmethacrylate] coated aqueous dispersed thermosensitive Fe_3O_4 nanoparticles. *J. Phys. Chem. C* 113, 10090 (**2009**).

36. N. Bhuchar, R. Sunasee, K. Ishihara, T. Thundat, and R. Narain, Degradable thermoresponsive nanogels for protein encapsulation and controlled release. *Bioconjug. Chem.* 23, 75 (**2011**).

37. J. M. Chan, L. Zhang, R. Tong, D. Ghosh, W. Gao, G. Liao, K. P. Yuet, D. Gray, J.-W. Rhee, and J. Cheng, Spatiotemporal controlled delivery of nanoparticles to injured vasculature. *Proc. Natl. Acad. Sci. USA* 107, 2213 (**2010**).

38. K. T. Nguyen, K. P. Shukla, M. Moctezuma, A. R. Braden, J. Zhou, Z. Hu, and L. Tang, Studies of the cellular uptake of hydrogel nanospheres and microspheres by phagocytes, vascular endothelial cells, and smooth muscle cells. *J. Biomed. Mater. Res. A* 88, 1020 (**2009**).

39. U. Westedt, L. Barbu-Tudoran, A. K. Schaper, M. Kalinowski, H. Alfke, and T. Kissel, Deposition of nanoparticles in the arterial vessel by porous balloon catheters: Localization by confocal laser scanning microscopy and transmission electron microscopy. *AAPS PharmSci.* 4, 206 (**2002**).

40. P. Li, P. Chevallier, P. Ramrup, D. Biswas, D. Vuckovich, M.-A. Fortin, and J. K. Oh, Mussel-inspired multidentate block copolymer to stabilize ultrasmall superparamagnetic Fe_3O_4 for magnetic resonance imaging contrast enhancement and excellent colloidal stability. *Chem. Mater.* 27, 7100 (**2015**).

41. I. Monaco, F. Arena, S. Biffi, E. Locatelli, B. Bortot, F. La Cava, G. M. Marini, G. M. Severini, E. Terreno, and M. C. Franchini, Synthesis of lipophilic core–shell Fe_3O_4@SiO_2@Au nanoparticles and polymeric entrapment into nanomicelles: A novel nanosystem for in vivo active targeting and magnetic resonance–photoacoustic dual imaging. *Bioconjug. Chem.* 28, 1382 (**2017**).

42. J. Qin, Q. Liu, J. Zhang, J. Chen, S. Chen, Y. Zhao, and J. Du, Rationally separating the corona and membrane functions of polymer vesicles for enhanced T2 MRI and drug delivery. *ACS Appl. Mater. Interfaces* 7, 14043 (**2015**).

43. X. Yu, T. Takayama, S. A. Goel, X. Shi, Y. Zhou, K. C. Kent, W. L. Murphy, and L.-W. Guo, A rapamycin-releasing perivascular polymeric sheath produces highly effective inhibition of intimal hyperplasia. *J. Control. Release* 191, 47 (**2014**).

44. S. Feng, Y. Hu, S. Peng, S. Han, H. Tao, Q. Zhang, X. Xu, J. Zhang, and H. Hu, Nanoparticles responsive to the inflammatory microenvironment for targeted treatment of arterial restenosis. *Biomaterials* 105, 167 (**2016**).

45. H. Zhang, K.-F. Ren, H. Chang, J.-L. Wang, and J. Ji, Surface-mediated transfection of a pDNA vector encoding short hairpin RNA to downregulate TGF-β1 expression for the prevention of in-stent restenosis. *Biomaterials* 116, 95 (**2017**).

46. T. Hara, D. Fukuda, K. Tanaka, Y. Higashikuni, Y. Hirata, S. Yagi, T. Soeki, M. Shimabukuro, and M. Sata, Inhibition of activated factor X by rivaroxaban attenuates neointima formation after wire-mediated vascular injury. *Eur. J. Pharmacol.* 820, 222 (**2018**).

47. J.-M. Daniel, J. Dutzmann, H. Brunsch, J. Bauersachs, R. Braun-Dullaeus, and D. G. Sedding, Systemic application of sirolimus prevents neointima formation not via a direct anti-proliferative effect but via its anti-inflammatory properties. *Int. J. Cardiol.* 238, 79 (**2017**).

48. B. Tesfamariam, Endothelial repair and regeneration following intimal injury. *J. Cardiovasc. Transl. Res.* 9, 91 (**2016**).

49. S. S. Ahanchi, N. D. Tsihlis, and M. R. Kibbe, The role of nitric oxide in the pathophysiology of intimal hyperplasia. *J. Vasc. Surg.* 45, A64 (**2007**).

50. M. J. Alef, R. Vallabhaneni, E. Carchman, S. M. Morris Jr., S. Shiva, Y. Wang, E. E. Kelley, M. M. Tarpey, M. T. Gladwin, and E. Tzeng, Nitrite-generated NO circumvents dysregulated arginine/NOS signaling to protect against intimal hyperplasia in Sprague-Dawley rats. *J. Clin. Invest.* 121, 1646 (**2011**).